

# A High Precision Fabry-Perot Cavity Polarimeter at HERA

---

**S. Baudrand, M. Bouchel, V. Brisson, R. Chiche, M. Jacquet, S. Kurbasov\*, G. Li†, C. Pascaud, A. Reboux, V. Soskov, Z. Zhang‡, F. Zomer**

*Laboratoire de l'Accélérateur Linéaire, Univ. Paris-Sud et IN2P3/CNRS,  
Orsay, France  
E-mail: zhangzq@lal.in2p3.fr*

**M. Beckingham§, T. Behnke, N. Coppola¶, N. Meyners, D. Pitzl, S. Schmitt**

*DESY  
Hamburg, Germany*

**M. Authier, P. Deck-Betinelli||, Y. Queinec**

*CEA, IRFU, SIS, Centre de Saclay  
Gif sur Yvette, France*

**L. Pinard**

*LMA, Université Claude Bernard LYON I et IN2P3/CNRS  
Villeurbanne, France.*

**ABSTRACT:** A Fabry-Perot cavity polarimeter, installed in 2003 at HERA for the second phase of its operation, is described. The cavity polarimeter was designed to measure the longitudinal polarisation of the HERA electron beam with high precision for each electron bunch spaced with a time interval of 96 ns. Within the cavity the laser intensity was routinely enhanced up to a few kW from its original value of 0.7 W in a stable and controllable way. By interacting such a high intensity laser beam with the HERA electron beam it is possible to measure its polarisation with a relative statistical precision of 2% per bunch per minute. Detailed systematic studies have also been performed resulting in a systematic uncertainty of 1%.

**KEYWORDS:** Polarimeter, Fabry-Perot cavity.

---

\*On leave of absence from P.N. Lebedev Physical Institute, Moscow, Russian Federation.

†Now at Institute of High Energy Physics, Chinese Academy of Science, Beijing, China.

‡Corresponding author.

§Now at Albert-Ludwigs-University Freiburg, Freiburg, Germany.

¶Now at European XFEL GmbH, Hamburg, Germany.

||Now at Synchrotron SOLEIL, Saint Aubin, France.

---

## Contents

<b>1. Introduction</b>	<b>1</b>
<b>2. Polarisation at HERA</b>	<b>2</b>
2.1 Polarisation Measurement - Polarimeters	3
2.2 Polarisation Measurement Modes	4
<b>3. Experimental Setup</b>	<b>5</b>
3.1 Design and Realisation of the Cavity for HERA	6
3.2 The Calorimeter	9
3.3 Electronics and DAQ	9
3.3.1 Feedback System	10
3.3.2 Calorimeter Fast DAQ System	10
<b>4. Determination of the Electron Beam Polarisation</b>	<b>13</b>
4.1 Principle of the Analysis Method	13
4.2 Detector Effects	14
4.3 Comparison of Measured and Theoretical Energy Spectra	15
<b>5. HERA Running and Cavity Data Taking</b>	<b>18</b>
<b>6. Results of Polarisation Measurement</b>	<b>20</b>
<b>7. Systematic Studies</b>	<b>23</b>
7.1 Uncorrelated Systematic Errors	24
7.2 Correlated Systematic Errors	24
7.3 Overall Systematic Uncertainty	25
<b>8. Summary</b>	<b>26</b>

---

## 1. Introduction

The electron<sup>1</sup>-proton collider HERA was upgraded after a first phase of data taking in years 1992 – 2000. The aim of the upgrade was to increase the luminosity by a factor of three and to provide a longitudinally polarised electron beam to the two general purpose detector experiments H1 [1] and ZEUS [2], in addition to the fixed target experiment HERMES [3].

---

<sup>1</sup>The term “electron” is used generically to refer to both electrons and positrons, unless otherwise stated.

To cope with the physics program after the upgrade, a fast and high precision longitudinal Compton polarimeter using a continuous wave laser resonating in a Fabry-Perot cavity (LPOL cavity) was proposed [4], constructed and installed near the existing longitudinal Compton polarimeter (LPOL) [5]. In addition to the LPOL, the transverse polarisation of the electron beam is also measured by another polarimeter (TPOL) [6].

With respect to the prior HERA LPOL and TPOL polarimeters, the higher statistical precision of the LPOL cavity is achieved by increasing firstly the power of the continuous wave laser by more than two orders of magnitude compared to the TPOL and secondly the frequency of the electron-photon(laser) interaction to 10 MHz compared to 0.1 kHz of the pulsed laser of the LPOL. A new Data Acquisition System (DAQ), synchronised to the HERA beam clock, has been developed accordingly which operates without any trigger at 10 MHz. This is one of the novelties of the experiment described in this article.

The HERA Fabry-Perot cavity is similar to a device that has been used successfully to measure the polarisation of the CEBAF LINAC electron beam [7, 8, 9]. One major difference between the HERA and CEBAF LPOL cavities is the dynamical regime. Whereas the luminosity of Compton scattering is relatively low at CEBAF, it reaches much higher values at HERA. That is, the average number of scattered Compton photons is close to one per bunch in the latter case and much smaller in the former. The HERA dynamical regime, denoted as ‘few photon mode’ in this article, has been used successfully for the first time by the LPOL cavity to measure the electron beam polarisation. An important point to mention is that a huge effort was made to reduce the unforeseen high level of synchrotron radiation emitted by the electron beam at the cavity location downstream of the HERMES experiment, by adding many protections (cf Sect. 3.1 for more detail) to avoid damaging any optical or electronic component [10]. Especially fragile were the ‘supermirrors’, whose high quality, which was maintained until the end of data taking, was the key to obtaining the foreseen high power of the laser,

The main purpose of this article is to describe the LPOL cavity experiment and to report about the electron polarisation measurement. The article is organised as follows: In Sect. 2, the principle of the electron beam polarisation measurement at HERA is discussed; In Sect. 3, the experimental setup of the LPOL cavity is described; Sections 4-7 are dedicated to the analysis method, the data taking, the polarisation results and the systematic studies, respectively, followed by Sect. 8 for summary.

## 2. Polarisation at HERA

Both the electron and proton ring of the HERA collider can have up to 220 bunches. Most of the electron and proton bunches are filled to allow the  $ep$  collisions. These are so-called colliding bunches. However, a small fraction of proton bunches are unfilled and thus the corresponding electron bunches have no partner. These are non-colliding or pilot electron bunches. The beam polarisation from both bunch types have to be measured.

In a storage ring like HERA, the electron beam has a natural transverse polarisation caused by emission of synchrotron radiation due to the bending magnetic field. This is the so-called Sokolov-Ternov (ST) effect [11]. The transverse polarisation arises from a small difference in the spin flip probabilities during a complete turn between the up-to-down ( $w_{\uparrow\downarrow}$ ) and down-to-up ( $w_{\downarrow\uparrow}$ ) flips. The

evolution of the spin up and spin down electron populations is given by

$$\frac{\partial \mathcal{P}_\uparrow}{\partial t} = -\frac{\partial \mathcal{P}_\downarrow}{\partial t} = w_{\downarrow\uparrow}\mathcal{P}_\downarrow - w_{\uparrow\downarrow}\mathcal{P}_\uparrow. \quad (2.1)$$

Solving this differential equation leads to the polarisation evolution

$$P(t) = P^\infty \left(1 - e^{-\frac{t}{\tau}}\right) \quad (2.2)$$

where

$$P(t) = \frac{\mathcal{P}_\uparrow - \mathcal{P}_\downarrow}{\mathcal{P}_\uparrow + \mathcal{P}_\downarrow}, \quad P^\infty = \frac{w_{\uparrow\downarrow} - w_{\downarrow\uparrow}}{w_{\uparrow\downarrow} + w_{\downarrow\uparrow}}, \quad \tau = \frac{C}{w_{\uparrow\downarrow} + w_{\downarrow\uparrow}} \quad (2.3)$$

with  $P^\infty$  and  $\tau$  being the maximum polarisation value and the intrinsic rise-time, respectively, and  $C$  is a constant depending on the ring parameters.

For a perfect flat HERA machine, where the polarisation of the beam is only due to the ST effect, one has asymptotically<sup>2</sup>  $P^\infty = P_{ST} = \frac{8}{5\sqrt{3}} = 92.4\%$  and  $\tau = \tau_{ST} \simeq 36.5 \text{ min}$  [13]. However as most of the physics at HERA is sensitive to longitudinal polarisation one needs to insert a device that transforms the transverse polarisation into longitudinal. This kind of device is called spin rotator and in the case of HERA a “Mini-Rotator” design, developed by Buon and Steffen [14], has been used. The spin rotators are located around the electron-proton interaction points and are installed in pairs allowing transversely polarised positrons to be rotated into longitudinally polarised states and back again.

These spin rotators are however responsible for a depolarisation which increases  $w_{\uparrow\downarrow}$  and  $w_{\downarrow\uparrow}$ . Nevertheless as the effect is mainly geometrical one expects that the difference  $w_{\uparrow\downarrow} - w_{\downarrow\uparrow}$  is largely preserved, meaning that  $P^\infty/\tau$  stays constant. The validity of this assumption may be tested by measuring the rise time and maximum polarisation in a rise-time experiment for both a flat and standard ring. For HERA it is expected that

$$\frac{P^\infty}{\tau} = \frac{P_{ST}}{\tau_{ST}} = 0.02532 (\text{min}^{-1}). \quad (2.4)$$

## 2.1 Polarisation Measurement - Polarimeters

Compton-laser polarimeters, widely used at  $e^+e^-$  storage rings (e.g. LEP [15], TRISTAN [16]), are based on the spin dependent cross section for Compton scattering of polarised photons on electrons. The longitudinal component of the electron polarisation is measured through the energy dependence of the cross section. The polarisation can be deduced from measurements of the final state electron [17, 18], but at storage rings it is more practical to detect the scattered photon. In this article we shall concentrate on the measurement of longitudinal polarisation of the electron beam.

Assuming a mono-energetic and mono-directional electron beam interacting with a laser beam, the number of scattered photons per unit of time and solid angle in the electron rest frame (with the  $z$  axis in the direction of motion of the electron beam) is given by [19, 6]

$$\frac{d^3 n_\gamma}{dt d\Omega} = \mathcal{L}_e \gamma C \left\{ \left[ 1 + \cos^2 \theta + 2(k_i - k_f) \sin^2 \frac{\theta}{2} \right] - [S_1 \cos 2\phi + S_2 \sin 2\phi] \sin^2 \theta \right\}$$

---

<sup>2</sup>Radiation depolarisation may result from quantum phase jumps [12].

$$\begin{aligned}
& - 2 \sin \theta \sin^2 \frac{\theta}{2} S_3 [P_y \sin \phi - P_x \cos \phi] \\
& - 2 \cos \theta \sin^2 \frac{\theta}{2} (k_f + k_i) S_3 P_z \Big\}, \tag{2.5}
\end{aligned}$$

with [20]

$$\mathcal{L}_{e\gamma} \approx \frac{1}{\sqrt{2\pi}} \frac{1 + \cos \alpha_{e\gamma}}{\sin \alpha_{e\gamma}} \frac{I_e}{ec} \frac{P_{\text{laser}} \lambda}{hc} \frac{1}{\sigma_{e,x}^2 + \sigma_\gamma^2} \quad C = \frac{1}{2} \left( \frac{e^2}{m_e c^2} \frac{k_f}{k_i} \right)^2, \tag{2.6}$$

where in Eq.(2.5),  $k_i$  and  $k_f$  are the momenta of the incident and scattered photons in the electron rest frame,  $\theta$  is the angle between the two and  $\phi$  the azimuthal angle in  $(x,y)$  plane perpendicular to the electron beam line axis  $z$ ;  $\cos \theta$  is univoquely related to the energy of the photon in the laboratory frame so that Eq.(2.5) also represents the scattered photon energy spectrum. The variables  $P_x$ ,  $P_y$  and  $P_z$  denote the three components of the electron polarisation vector in the  $x$ ,  $y$  and  $z$  directions. The circular photon polarisation is described by the third component  $S_3$  of the Stokes parameters  $(S_1, S_2, S_3)$  [19]. The electron beam-laser beam luminosity  $\mathcal{L}_{e\gamma}$  is given in Eq.(2.6) and the other parameters in Eq.(2.6) are the electron-laser crossing angle  $\alpha_{e\gamma}$ , the electron beam current  $I_e$ , transverse beam size  $\sigma_{e,x}$  in  $x$ , the laser beam power  $P_{\text{laser}}$ , wavelength  $\lambda$ , beam size  $\sigma_\gamma$ , the electron electric charge  $e$ , mass  $m_e$  and the speed of light  $c$ .

Since the nominal HERA electron beam energy is around 27.5 GeV, much larger than that of the laser beam, the photons are scattered within a tiny cone of a few hundreds of micro-radian in the direction of the electron beam. Therefore the photon energy distribution can be measured within a small calorimeter.

The three components of the electron polarisation appear only in the third and fourth lines on the right-hand side of Eq.(2.5) and are connected with the circular laser polarisation component  $S_3$  only. Therefore for a precise determination of the electron polarisation, one needs to maximize the level of circular laser polarisation ( $S_3 \rightarrow \pm 1$ ). Knowing  $S_3$ , the electron longitudinal polarisation  $P_z$  can be determined by a fit to the distribution of the scattered photon energy. To determine the transverse polarisation, one has to measure both the energy distribution and the azimuthal angle  $\phi$ .

## 2.2 Polarisation Measurement Modes

At HERA, where the electron bunches are separated by  $\Delta t = 96$  ns in time, the number of back-scattered Compton photons (hereafter named BCP) per bunch is given by  $n_\gamma = \Delta t \int d\Omega (d^3 n_\gamma / dt d\Omega)$ . Depending on the value of  $n_\gamma$ , one can define three different measurement modes: (1) single photon mode ( $n_\gamma \ll 1$ ), (2) few photon mode ( $n_\gamma \approx 1$ ) and (3) multi-photon mode ( $n_\gamma \gg 1$ ). These are the operation modes of the TPOL [6], the LPOL cavity and the existing LPOL [5] respectively.

The advantage of the single photon mode is that one can calibrate the calorimeter in an absolute way using two reference points of the photon energy spectrum independently of the electron beam polarisation: firstly the Compton kinematic edge, located at 10 GeV at HERA for a 1064 nm laser beam wavelength, and secondly the bremsstrahlung kinematic edge, located around 27.5 GeV which corresponds to photons radiated from the scattering of the electron beam with the residual gas of the vacuum beam pipe (hereafter named BGP). The disadvantage of the single photon mode is the low statistics. In the case of the TPOL, a 10 W laser with green light is used, corresponding to  $n_\gamma \approx 0.01$  per bunch.

The multi-photon mode becomes advantageous when the background is large. The LPOL uses a high energy pulsed laser and typically a thousand photons per bunch are produced per laser-beam interaction. This corresponds to about 10TeV energy measured in the calorimeter. The disadvantage is thus related to the energy linearity of the calorimeter which is only calibrated at low energy. The statistics are also limited by the laser pulse frequency (100Hz for the LPOL).

With respect to these two modes, the determination of the longitudinal polarisation in the few photon mode is more involved since one has to consider a Poissonian superposition of BCPs resulting in a complex energy spectrum (one observes the total energy in the calorimeter which can be made of many combinations of few BCPs as well as background photons). The BCP energy spectrum is thus given by multiple convolutions of the one BCP energy distribution of Eq.(2.5) and therefore becomes a non-linear function of the electron beam polarisation. However, the advantage of the few photon mode is threefold: firstly the statistics are larger, secondly the signal over background ratio is higher than that of the single photon mode and finally the multiple kinematic edges, which are independent of the electron beam polarisation, can be used to calibrate the calorimeter and determine eventually the non-linearity of the energy measurement.

The main result of this article is the experimental demonstration of high precision measurement of the HERA electron beam polarisation in the few photon mode.

### 3. Experimental Setup

In order to reach the few photon mode with the given HERA electron beam current, one has to use a continuous laser beam of a few kilo Watt power. At the time when the experiment was designed (1999-2000), the only way<sup>3</sup> to reach such a high power was to use a Fabry-Perot optical resonator [4, 23] fed by a continuous laser beam.

Fabry-Perot cavities are a widely used optical device. Since their properties are described in many textbooks (e.g. [23]), only their main characteristics are mentioned here. The cavity of our experimental setup consists of two identical spherical mirrors of very high reflectivities  $R > 0.999$ , where  $R$  is the reflection coefficient for the beam intensity. Now, considering the simple case of an optical plane wave, an optical resonance occurs when the length between the two mirrors  $L$  is equal to an integer number,  $q$ , times the laser beam wavelength  $\lambda$ . Denoting the laser beam frequency by  $\nu_L = c/\lambda$ , this condition reads  $\nu_L = q \times \text{FSR}$  where  $\text{FSR} = c/(2L)$  is the cavity Free Spectral Range. Small corrections to this resonance condition appear [4] when one considers the eigenmodes of the resonator. But in any case, when this condition is fulfilled, the incident laser beam power  $P_{\text{laser}}$  is enhanced inside the cavity by a factor  $F/\pi$ , where  $F = \pi\sqrt{R}/(1-R)$  is the cavity finesse. However since the resonance Full Width at Half Maximum (FWHM) is defined by  $\text{FWHM} = \text{FSR}/F$ , the highest  $F$  (and hence the highest enhancement factor) leads thus to the smallest FWHM. This means that in order to keep the system at resonance, one must control the value of  $\nu_L$  with a relative precision better than  $\text{FWHM}/(q \times \text{FSR})$ . For the 2m long cavity and Nd:YAG laser ( $\lambda = 1064\text{nm}$ ) used in the cavity polarimeter and described in the next section, one gets  $\text{FWHM}/\nu_L \approx 10^{-11}$ . This is the precision needed for matching the cavity length and the laser

---

<sup>3</sup>Indeed, neither the very high power fiber lasers [21] nor the locking of mode locked (pulsed) laser beams to high finesse Fabry-Perot cavities [22] were available or, at least, reasonably conceivable.

beam wavelength to maintain the cavity in resonance. This is done with a feedback system acting on the laser beam frequency, and by using a monolithic cavity.

In practice, the cavity enhancement factor can be reduced by three main sources: an error in the mode matching of the transverse mode of the laser to the fundamental Gaussian mode of the cavity [23] (which can be induced, for example, by misalignments [24]); an error in the frequency feedback (which can happen, for example, because of a wrong estimation of the feedback bandwidth with respect to the laser or cavity frequency noise density spectra); some differences between the optical properties of the two cavity mirrors. The measured coupling between the laser beam and the cavity was about 70% during the operation in the HERA tunnel.

### 3.1 Design and Realisation of the Cavity for HERA

The experimental setup of the cavity polarimeter consists of a laser and other optical components inside or close to a Fabry-Perot cavity, built around the HERA electron beam pipe. This provides circularly polarised photons which interact with electrons from the main beam of the HERA collider, about 100 meters away from the HERMES experiment. This setup is complemented by a calorimeter, about 60 meters downstream of the cavity, for detecting and measuring the BCPs.

A schematic view of the monolithic cylindrical cavity vessel, with its two mirrors around the electron beam pipe separated by a distance of about 2 m from each other, is illustrated in Fig. 1. The cavity mirrors, with a 2 m curvature radius (confocal cavity [23], the most stable from the mechanical point of view), were installed as close as possible to the beam pipe, to minimize the electron-laser beam crossing angle (3.3 degrees). The laser and all other optical components were located on an optical table outside of the cavity.

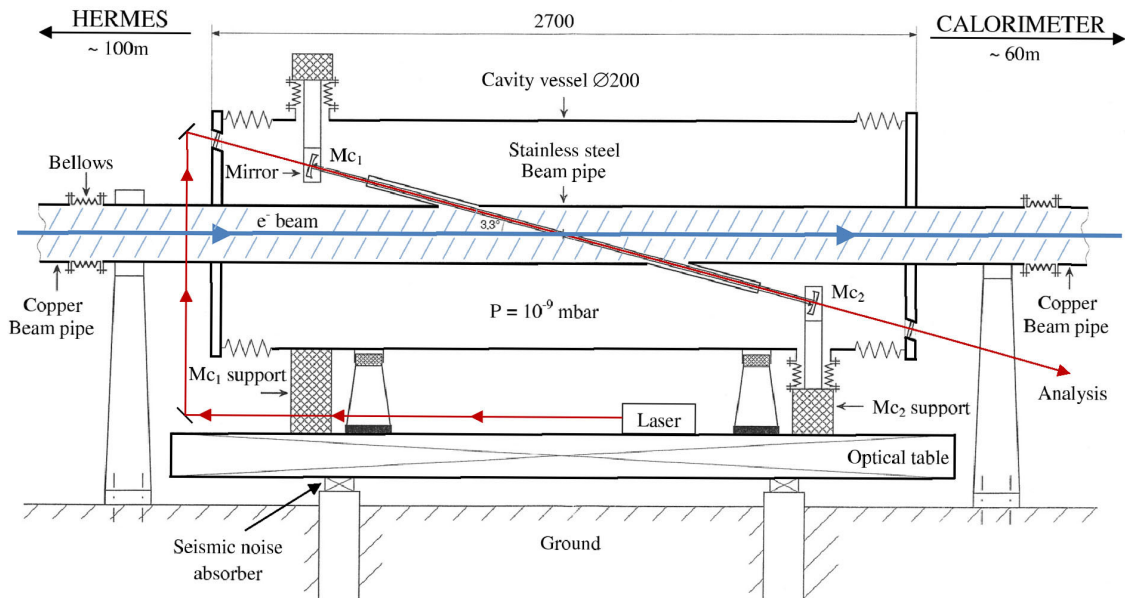


**Figure 1.** Scheme of the cavity surrounding the electron beam pipe with the laser and main mirrors.

For installing such a cavity around a ring accelerator beam pipe, two main difficulties arise:



the presence of the wake field from the electron beam and the presence of vibrations in the whole tunnel environment. The wake field from the circulating electron beam should not disturb the cavity operation, and the cavity should not affect the electron beam. The propagation into the cavity of high frequency modes from the passing beam is suppressed by introducing two 15 mm diameter metallic tubes around the laser beam extending to a length of  $\pm 80$  cm from either side of the holes in the beam pipe. A simulation has shown that this reduces the electron beam power loss through electromagnetic heating to an almost negligible level (18 W during injection, less than 0.1 W during normal beam operation <sup>4</sup>). Optical calculations, further confirmed experimentally, have also shown that the tubes do not perturbate the cavity resonance conditions.

Another important requirement of the whole device is a very good mechanical stability with time. This means essentially no vibrations and a small temperature variation. The overall realisation is shown in Fig. 2. The whole optical setup, including the cavity mirrors, is vibration isolated: the beam pipe inside the cavity vessel, attached to the cavity end-flanges, is isolated from the rest of the beam pipe by two standard HERA bellows sitting outside the cavity, and from the cavity vessel by two other big bellows; the optical table feet are equipped with elastomer isolators to cut vibrations from the tunnel ground, and passive elastomer absorbers to isolate the table from all items in contact (cavity vessel, vacuum pumps etc); the mirror mounts are rigidly clipped on the optical table and are linked to the vessel through metal bellows thus filtering the remaining vibrations. In this way, the cavity mirror holders are completely part of the optical table which supports all the optics. The mirror mounts are able to be rotated manually in all directions while keeping the mirror centre position fixed.

To control the thermal expansions of the cavity and of the optical table, the whole system is surrounded by an isotherm house shielded by a 3 mm lead sheet to protect the system against synchrotron radiation. In addition, a thick lead protection has been installed around the beam pipe outside the cavity, and in front of the cavity. The laser has been surrounded by a big mu-metal, steel and lead bunker. Inside this house, the temperature is controlled and kept constant to well within  $\pm 1^\circ\text{C}$  via heating ribbons and feedback sensors.

A schematic view of the optical scheme is shown in Fig. 3. Apart from the cavity, there are two main parts: the entrance for providing the laser beam in the cavity and the output for measuring the polarisation of the laser beam.

The laser source is a commercial non-planar ring Nd:YAG oscillator [25] from the Lightwave company. The laser beam frequency can be modified in two ways:

1. A piezo-electric transducer is located on the laser rod, thereby modifying the rod geometry and therefore the laser beam frequency. This is a fast and fine tuning: the laser beam frequency changes by 3.4 MHz per Volt applied on the actuator within a bandwidth of  $\approx 30$  kHz.
2. The rod temperature can be varied thanks to a Peletier module (controlled by a DC voltage). This temperature variation induces a change of the laser beam frequency of 5 GHz per Volt applied on the Peletier module. This is a slow frequency variation with a bandwidth of  $\sim 1$  Hz.

---

<sup>4</sup>Estimated by S. Wipf from the DESY accelerator group.





**Figure 2.** Picture of the cavity taken during the installation. The laser and the optical elements before the cavity entrance are located on the rail parallel to the cavity vessel.

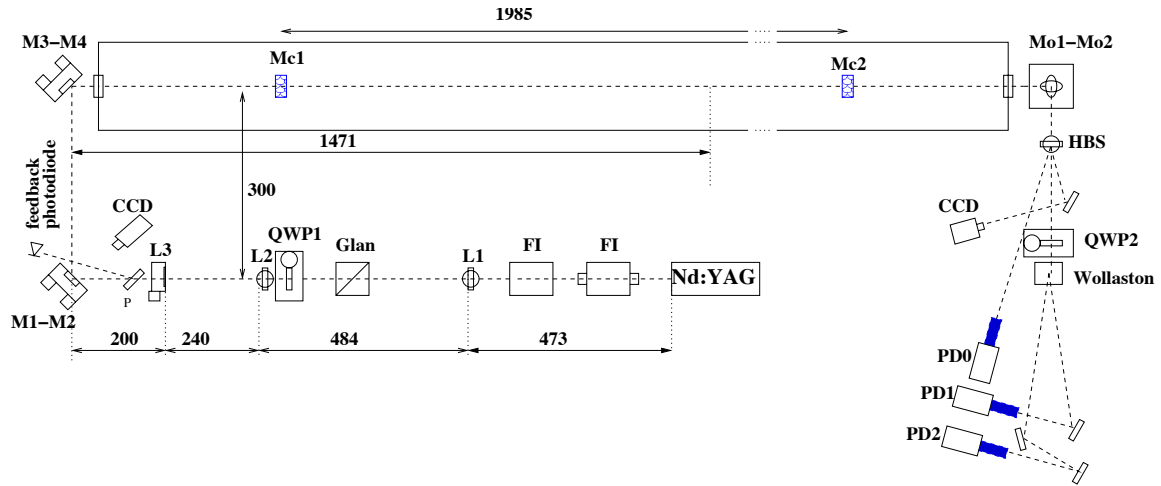


**Figure 3.** Schematic view of the optical scheme. The scales are shown in mm.

The optical scheme at the entrance of the cavity is designed to fulfill the five different functions: (a) isolation of the laser oscillator, with a double stage Faraday Isolator (FI), a Glan-Thomson

prism is used to get a purely linearly polarised state; (b) obtaining a circular polarisation of the laser beam and switching between left and right circular polarisation by using a fast and precise remotely controlled rotating quarter wave plate (QWP1 or MOCO); (c) laser/cavity mode matching, using three lenses (L1, L2, L3); (d) extraction of the cavity-reflected photon beam to be used for the feedback system; (e) laser/cavity geometrical alignment using four flat  $45^\circ$  dielectric mirrors M1, M2, M3 and M4.

The laser beam enters and exits the cavity vessel through vacuum windows. The two cavity spherical mirrors (Mc1 and Mc2), with one inch diameter and 2m curvature radius, are coated for 1064nm wavelength with several  $\text{Ta}_2\text{O}_5/\text{SiO}_2$  quaterwave stacks. The coating losses (due to diffusion and absorption) are very small ( $\approx 1.5 \times 10^{-6}$ ), and the transmission coefficient amounts to  $T = 1 - R \approx 10^{-4}$ . The finesse of the cavity, calculated and measured as 30000, remained constant until the end of the data taking period.

An ellipsometer located at the output of the cavity is used to measure the laser beam polarisation. It is described in details in a companion article [26] to the present one. The principle of the measurement is to send a light beam of any unknown polarisation through first the QWP1 and then the cavity, and from there it is guided with two mirrors (Mo1 and Mo2) to go through a holographic beam sampler (HBS) and another quarter wave plate (QWP2). By rotating this latter plate, the polarisation state of the light is modified and the state at the exit of the plate depends on the state at the entrance. A polariser (Wollaston prism) placed behind the plate spatially separates the beam into two orthogonal linearly polarised states. The analysis of the intensities of these two beams in photo-detectors (PD1 and PD2 with PD0 being used as a reference), for various azimuthal angles of the QWP, allows the deduction of the polarisation of the incident beam.

### 3.2 The Calorimeter

A sampling calorimeter [27] was used to measure the energy spectrum of the back-scattered Compton photons as well as photons from background processes. It was located on a movable table which can be remotely moved away from the photon beam line during the beam injection and may be used to optimise the rate of measured BCPs during the data taking. The calorimeter has a total of 24 layers where each layer consists of a 3.0mm tungsten (W) absorber plate and a 2.63mm scintillator plate. The plates are  $40 \times 40 \text{ mm}^2$  and are optically coupled on all four sides to wavelength shifter (WLS) plates that bring light to one Photo Multiplier Tube (PMT) placed at the back of the calorimeter behind a 27mm W shielding plate. The PMT transmutates the light from the WLSs into an electrical signal. The calorimeter response has been simulated [27] using the Monte Carlo program GEANT3 [28].

The energy resolution and uniformity have been measured in test beams at DESY. The measured energy resolution  $\sigma/E = a/\sqrt{E(\text{GeV})} \oplus b$ , with  $a = 16.0\%$  and  $b = 0.3\%$ , is in agreement with the Monte Carlo simulations. The uniformity scan showed less than 5% deviation from linearity for up to  $\pm 10 \text{ mm}$  from the calorimeter centre. The linearity is measured to about 0.2% over the full energy range of 1 to 6 GeV of the test beams.

### 3.3 Electronics and DAQ

For the polarisation measurement two electronic systems are designed. The first one is the feedback system which locks the laser frequency on one of the Fabry-Perot cavity harmonics, and the second

one is the scattered photon readout system. We shall first describe briefly the cavity feedback system and then concentrate on the fast calorimeter DAQ, the main novel aspect of our electronic readout system.

### 3.3.1 Feedback System

The feedback system (Fig. 4) is based on the Pound-Drever-Hall (PDH) method. We modulate the incident photon beam at 930 kHz in order to create two sidebands. The modulation frequency is much higher than the bandwidth of the cavity. When the main laser frequency is near a Fabry-Perot harmonic, the main part of the photon beam is absorbed but the sidebands are reflected. This reflected beam is processed to obtain the error signal for the feedback.

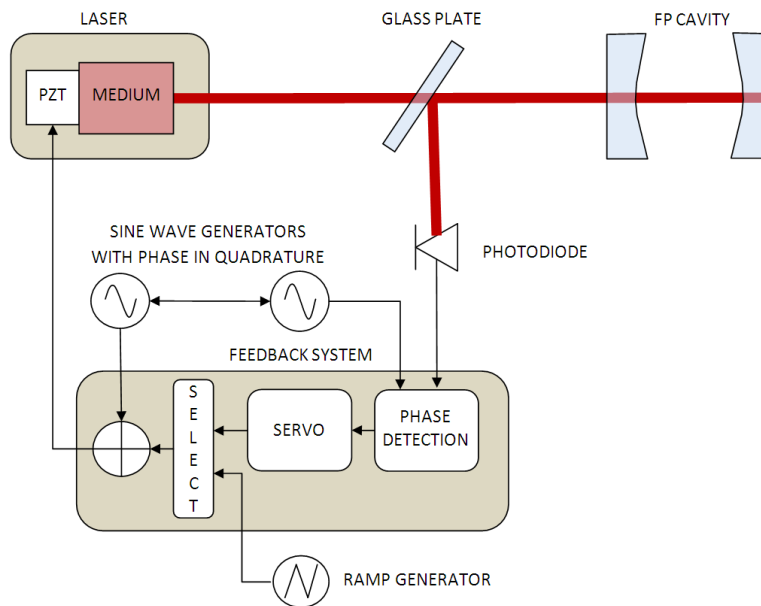


**Figure 4.** Simplified view of the feedback system (see text).

The feedback system works in 2 steps:

- The first step is to find a resonance frequency. The system selects the ramp generator which is applied to the laser PZT. The laser frequency shifts slowly and can cross one of the cavity resonance frequencies.
- Once a resonance frequency is reached, the feedback system switches and closes the feedback loop. An analog filter of many orders allows to maintain the cavity resonance.

### 3.3.2 Calorimeter Fast DAQ System

The DAQ hardware components (Fig. 5) are similar to those used for the electronic upgrade of the HERA transverse polarimeter and for the new H1 luminometer [29]. The main difference lies in the fact that the cavity polarimeter does not use any trigger to reduce the event rate. Therefore the DAQ system has to be fast enough to cope with the HERA bunch frequency of 10.4 MHz.

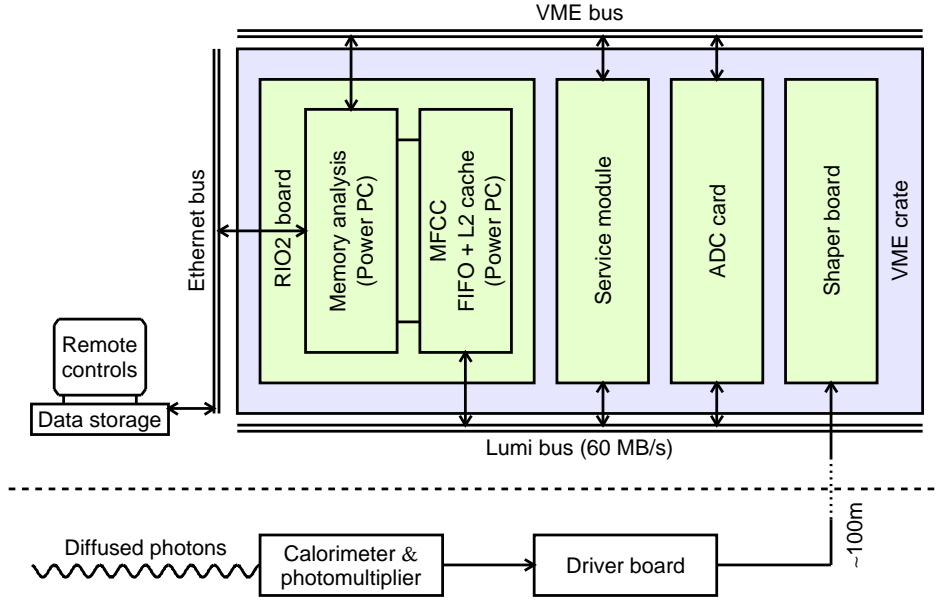


**Figure 5.** Global architecture of the DAQ system.

The energy spectrum of the emitted photons is measured in terms of charges collected in the tungsten-scintillator sampling calorimeter and read out by a photomultiplier. A driver board is used to amplify the signal before being sent along  $\sim 100$  m of cables to a shaper board. A dummy channel is also sent along the cables for the subtraction of the common noise by the shaper board. Due to the long cable length, the signal has very long tails due to the skin effect, thus the signal is optimized to have the much longer signals in 96 ns (10.4 MHz) to reduce sensitivity to jitter by overdriving some high frequencies.

The shaped output is fed to an ADC card in the form of a differential signal up to 2 V, with a return to the baseline below 1% in 96 ns. The fast shaping is essential to avoid electronic pileup from one bunch to the next.

The digital part of the acquisition system fits in a standard 22-slot VME crate. It includes the ADC card, a service module which drives all clocks in the system and a commercial Power-PC processor board composed of a VME mother board RIO2 8062<sup>5</sup> and a PCI (Peripheral Component Interconnect) connected daughter board MFCC 8442<sup>6</sup>, both from CES [30]. A dedicated 14-slot wide fast readout bus backplane is used to transfer signals between these boards.

The ADC card digitizes the analog signal from the shaper board in 12 bits at 41.6 MHz and stores 4 samples per bunch crossing in 2 independent pipelines of a depth of 512 samples each. One is readable via the VME bus and the other via the fast readout bus.

The service module receives the HERA clock (96 ns) and the machine cycle (first bunch) signal. It provides two internal clocks, which are 2 and 4 times faster than the HERA clock, to drive

<sup>5</sup>RIO stands for Reduced instruction set computer I/O, RIO2 8062 board has a 603r Power-PC of 300 MHz.

<sup>6</sup>Multi-Function Computing Core card 8442 contains a 7400 Power-PC of 466 MHz, a 128 Mbyte SDRAM (Synchronous Dynamic Random Access Memory), a 64-bis Power-PC bus of 66 MHz, a 1 Mbyte level 2 cache and two fast FPGA (Field-Programmable Gate Array) of Altera 10K50.

the ADC sampling clocks and does the phase adjustment between the ADC samples and HERA clock. The phase is adjusted such that the maximum signal corresponds to the second ADC sample and the baseline to the fourth sample. The difference of the two thus gives the signal amplitude. Note that, since the fast readout bus transfers two ADC samples together in 24 bits, there is an ambiguity in the second and fourth ADC samples. Due to this, the maximum can be either in the second sample and the baseline in the fourth one or vice versa, depending on the exact moment when the DAQ program is started.

The readout sequence and bus protocol are controlled by a FPGA (Field-Programmable Gate Array) located on the MFCC board. The core of the fast acquisition program runs into the MFCC Power-PC attached to the RIO2 Power-PC and consists of two nested loops. The outer loop runs on a requested number of HERA turns (default is 400000), the inner loop runs on the 220 bunches with 4 times 12-bit samples per bunch for one HERA turn.

The data from the ADC pipeline is added to the FIFO (First In First Out) of the front-end FPGA of the MFCC board through the fast readout bus in 24 bits every 20.8MHz. The data in the FIFO are packed in a 64-bit format (4 times 12 bits plus status bits) which corresponds to 4 ADC samples (1 bunch). A block of  $4 \times 64$ -bit FIFO data is then transferred through the 64-bit Power-PC bus at 66MHz to a 1-Mbytes level 2 (L2) cache of the MFCC. A whole HERA beam turn of 220 bunches needs thus 55 of such transfers. In the cache, for every one of 220 bunches, a histogram is created and filled using by default the difference of the second and fourth ADC samples.

The L2 cache may accommodate 220 histograms each containing 1024 bins with a maximum bin content of 65535 (16 bits). The gain of the analog chain is chosen in order to get a full dynamic range of about 90GeV. The histogram bins are then scaled down to 512 bins whereas the bin content is expanded to 32 bits (maximum content is increased to  $4 \times 10^9$ ) to avoid potential overflow in the bin content. In an improved version of the histogramming code, three variable bin sizes are further used to store in an optimal way the energy distribution for the given 512 bins: finer bin size at low energies which contain both the high statistics and the BCP signals and two coarser bin sizes at medium and high energies.

Since there is no hardware synchronisation between the HERA clock and the histogram filling, a system of waiting loops is implemented in the acquisition code to perform the matching and to avoid full or empty FIFO issues. Once the requested amount of data (400000 HERA turns) is reached, the histograms are transferred to the Power-PC of the RIO board via a PCI bus and the memory is refreshed. The transfer takes less than 100ms before another acquisition cycle can start. Two successive cycles correspond to two different circular laser polarisations; one left handed and the other right handed. The matching between a given laser polarisation state and the corresponding histograms is ensured in the acquisition code.

The histogram data are sent through the local network into a dedicated PC for online processing and publishing of results on the DESY network, as well as for storage for subsequent offline analysis. On the same PC, the DAQ program can be started and stopped remotely from any other PC connected to it.

## 4. Determination of the Electron Beam Polarisation

### 4.1 Principle of the Analysis Method

The available data for the polarisation measurement of an individual bunch consists of a pair of photon energy histograms each with 512 bins. These are successively recorded by the calorimeter DAQ for each bunch during one DAQ period ( $\approx 10$  s) for the two polarisation states of the laser beam  $S_3 = +1$  and  $S_3 = -1$ . These spectra come from a sum of genuine BCPs from electron-laser interactions, and three main backgrounds: the already mentioned BGP, the electron beam scattering off Black Body Photons (BBP) emitted by the hot beam pipe and the Synchrotron Radiation Photons (SRP).

Each histogram provided by the calorimeter DAQ is thus a set of integer numbers  $\{h_i\}_{i=1,\dots,512}$  in a measured energy interval  $[E_{i-1}, E_i]$  for a given bunch. Since the DAQ operates without trigger, the total number of entries of the histograms are fixed to the number of HERA turns  $N_{\text{loops}}$  accumulated during one DAQ period  $\sum_i h_i = N_{\text{loops}} = 400000$ . This constraint is necessary if one wants to extract precisely the electron beam polarisation for all bunches from a fit to a pair of two histograms corresponding to  $S_3 = +1$  and  $S_3 = -1$  laser polarisation states in the few photon mode.

The numerical procedure that has been set up to extract the polarisation from the bunch energy histograms is the following:

- The theoretical energy spectra of one BCP (see Eq.(4.2)), BGP and BBP [31] are computed numerically (the SRP background is considered as a pedestal and it is treated separately as described below).
- All these spectra are mixed to provide an energy histogram according to the method described below.
- The detector effects (calorimeter, ADC/energy conversion and electronic noise) are applied to the energy histograms.
- A comparison between the experimental and calculated energy histograms is performed using a likelihood fit. The unknown parameters of this fit are the luminosities of the BCP, BGP and BBP processes integrated over one DAQ period, the electron beam polarisation and the parameters describing the detector effects.

It was verified numerically that, as mentioned in Sect.2.2, the simultaneous determination of the electron beam polarisation and the other parameters can be obtained since the energy histograms possess kinematic edges independent of the electron and laser beam polarisations.

A detailed derivation of the formula used in our fits can be found in [31]. Here we just indicate the main ingredients of the method. This analysis method uses probabilities which are discretised. The probability  $p_i$  for a photon to be in the energy bin  $i$  is computed from the theoretical differential cross sections and includes the following independent contributions:

$$p_i = a_{\text{BCP0}} \times p_{i,\text{BCP0}} + a_{\text{BCP1}} \times p_{i,\text{BCP1}} + a_{\text{BGP}} \times p_{i,\text{BGP}} + a_{\text{BBP}} \times p_{i,\text{BBP}} \quad (4.1)$$

where  $\sum_i p_{i,x} = 1$  with  $x$  representing the different processes,  $a_x$  depend on the luminosities of the corresponding processes and BCP0 and BCP1 are related to the BCP differential cross sections,



independent of and linearly dependent on the product  $S_3 P_z$  respectively

$$\frac{d\sigma_{\text{BCP}}}{dE_{\text{BCP}}} = \frac{d\sigma_{\text{BCP0}}}{dE_{\text{BCP}}} + S_3 P_z \frac{d\sigma_{\text{BCP1}}}{dE_{\text{BCP}}} \quad (4.2)$$

where the energy spectra  $d\sigma_{\text{BCP0}}/dE_{\text{BCP}}$  and  $d\sigma_{\text{BCP1}}/dE_{\text{BCP}}$  are derived from Eq.(2.5).

The expression for the total (theoretical) energy follows the Poissonian law and can be written as:

$$P_i = \sum_{N=0}^{\infty} e^{-M} \frac{M^N}{N!} \delta \left( E_i - \sum_{k=0}^N E_{i_k} \right) \sum_{i_1} p_{i_1} \cdots \sum_{i_k} p_{i_k} \cdots \sum_{i_N} p_{i_N} \quad (4.3)$$

where  $M = a_{\text{BCP0}} + a_{\text{BCP1}} + a_{\text{BGP}} + a_{\text{BBP}}$  is the average number of expected photons entering the calorimeter per bunch crossing (the SRP being treated separately);  $N$  is the number of scattered photons (in practice it turns out that  $N \leq 5$  is enough in our dynamical regime); indices  $i_k$  run over all the bins of the theoretical histogram.

Note that Eq.(4.3) is indeed the sum of the discrete  $N^{\text{th}}$  convolutions of the energy histograms so that one can identify the contribution  $N = 0, N = 1, N = 2, \dots, N = 5$  to the zero-photon (i.e. the SRP peak), one-photon, two-photon, ..., five-photon energy spectra.

The probability to get a histogram  $\{h_i\}_{i=1,\dots,512}$  is finally given by:

$$\mathcal{P} = \prod_i (P_i)^{h_i} \quad (4.4)$$

from which the likelihood estimator may be extracted:  $\mathcal{W} = -2 \ln(\mathcal{P})$ . The likelihood minimization procedure is standard (see [31] for further details).

If the SRP background would have been included in the above formula, the number of terms in Eq.(4.3) would have been very large (from 500 to 150000 photons with the critical energy of  $\approx 40$  keV and the peak energy ranging from 20 MeV to 6 GeV). The adopted solution is to introduce a term in Eq.(4.3) that combines (adds) the SRP distributions into a so-called (Gaussian) radiation peak, as described in Sect. 4.2. The result shows a very narrow distribution in the energy region where no other photon is present.

## 4.2 Detector Effects

The detector response effects that are taken into account are not explicitly shown in the probabilities of Eq.(4.3). Indeed, the calorimeter has been simulated with GEANT3 [28] in order to derive a parameterisation describing the energy response. In addition to the calorimeter response to BCP or BGP photons, a specific study has also been devoted to the SRP which corresponds to, as indicated in the previous section, a large number of low energy photons. From the simulation studies, it turns out that the calorimeter response function  $f_E(E, E_0)$ , relating the energy  $E$  observed in the calorimeter to the ‘true’ incident energy  $E_0$ , can be modeled by the following quasi Gaussian distribution

$$f(E, E_0) dE = \frac{e^{-x} x^{\delta-1}}{\Gamma(\delta)} dx \quad (4.5)$$

where  $E = \alpha x^\mu E_0$ ,  $\alpha$  and  $\delta$  are given by  $\langle E/E_0 \rangle = \alpha \delta$  and  $\sigma_E^2 = \alpha^2 \delta$ , and  $\Gamma$  is the special Gamma function. Note that such a distribution approximates to a Gaussian if  $E_0/\sigma \rightarrow 0$  and vanishes when  $E \leq 0$ , which is not the case for a true Gaussian. For  $\mu = 1$  it also shares with a Gaussian the



calorimeter additive property  $\sigma_{E_1}^2 + \sigma_{E_2}^2 = \sigma_{E_1+E_2}^2$ . However a more versatile ansatz with  $\mu \neq 1$  has been used to better approach the simulation especially at low  $E_0$ . The functional forms of  $\mu(E_0)$  and  $\alpha(E_0)$  have been derived from the simulation studies. They depend on five free detector parameters which are determined from the likelihood fit to the data.

Finally, the conversion of the number of ADC counts  $N_{\text{ADC}}$  to energy is described by

$$N_{\text{ADC}}^i \propto \frac{E_i/r}{1 + \frac{d_{\text{bias}}}{E_i} + s_{\text{bias}}E_i} \quad (4.6)$$

where  $r$  stands for an energy response factor which may be time dependent and  $E_i$  is the energy in histogram bin  $i$ ,  $d_{\text{bias}}$  takes into account the fact that the calorimeter is less efficient for energies below 1 GeV (the simulation gives  $d_{\text{bias}} = 0.035 \text{ GeV}$ ), and  $s_{\text{bias}}$  has been added to take care of a possible leakage (usually very small) given by a photon beam misalignment with respect to the calorimeter center. These three parameters are also determined from a fit to the experimental histograms.

Note that other models for the detector response have also been considered in order to evaluate the systematic uncertainty related to the choices of Eqs.(4.5) and (4.6) (see Sect. 7).

The method developed in the analysis is to determine the relevant detector parameters by minimising the likelihood estimator  $\mathcal{W}$  using the energy spectra selected from some specific datasets and bunches (see Sects. 5 and 7.1).

It was checked numerically that the measured energy spectra allows an in-situ determination of the characteristics of the calorimeter independently of the electron beam polarisation. This over-constrained feature of the Compton spectra in the few photon mode turned out to be crucial for the polarisation measurements, since the calorimeter could not be calibrated with a high energy test beam before its installation and in addition it is subject to aging effects. Indeed, as it is shown in Fig. 6, the energy response factor  $r$  and resolution  $a$  of the calorimeter determined from the fit to the energy spectra vary as a function of the radiation dose (which is proportional to the number of data samples taken by the LPOL cavity). The energy resolution  $a$  was found to be worse than the test beam result (Sect. 3.2). This is due to the degradation caused by aging effects and the addition of a  $2X_0$  tungsten plate in front of the calorimeter for reducing the synchrotron radiation.

### 4.3 Comparison of Measured and Theoretical Energy Spectra

Taking the cross sections for BCP, BGP, and BBP shown in [31], the whole experimental setup has been modeled. The resulting energy spectra have been computed for every individual process emitting one or more photons, and two processes convoluted together. Finally, the convolution of all the processes has been performed. These curves are shown in Fig. 7 and compared to a measured energy distribution. An excellent agreement is seen between the data and curve (8) representing the sum of all processes. The BBP component is not shown explicitly but included in the sum in Fig. 7. From this typical experimental spectrum, one can clearly see that the contribution of three photons is already at the percent level and that the two photon contributions reproduce the various kinematic edges which appear as small local maxima in the energy spectrum. Note that the various contributions are convoluted with the detector response.

In Fig. 8, the two spectra for laser polarisation  $S_3 = 1$  (full dots with the full curve) and  $S_3 = -1$  (open dots with the dashed curve) are shown, together with the measured values in the ‘Compton

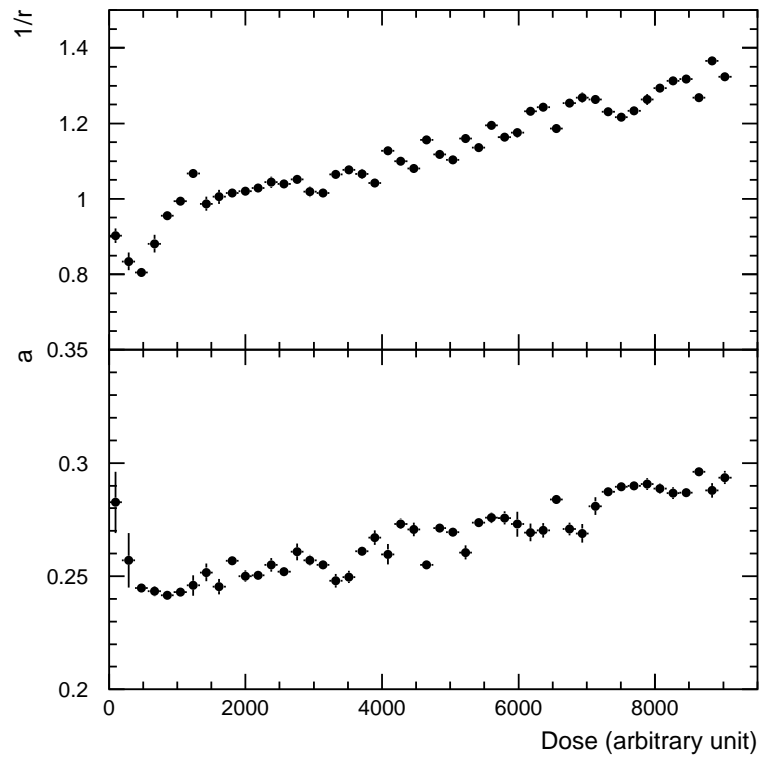


**Figure 6.** Observed variation of the calorimeter energy response factor ( $r$ ) and resolution ( $a$ ) as a function of radiation dose in an arbitrary unit.

energy range'. The difference allows the electron polarisation measurement, as mentioned previously.

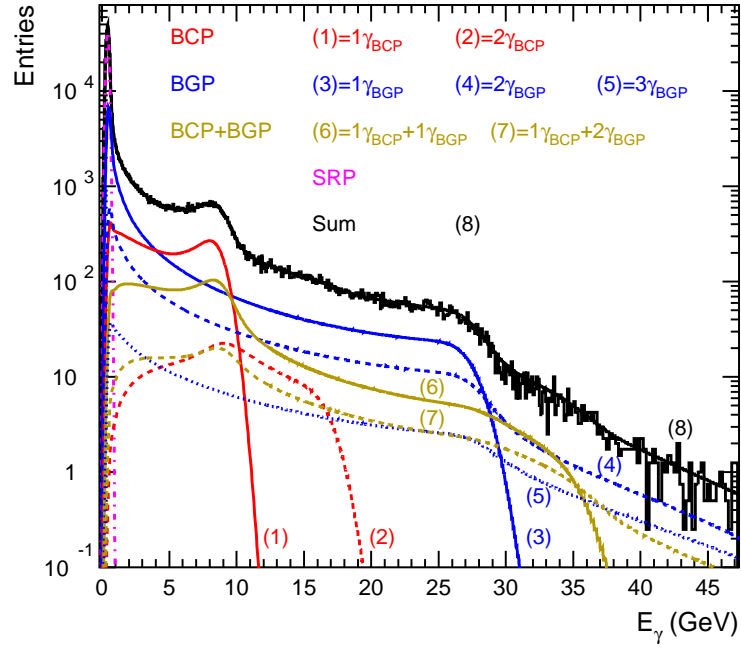


**Figure 7.** A measured energy spectrum (histogram) of a given bunch shown together with different contributions obtained from predictions (curves). The data were accumulated during about 10s of acquisition time.

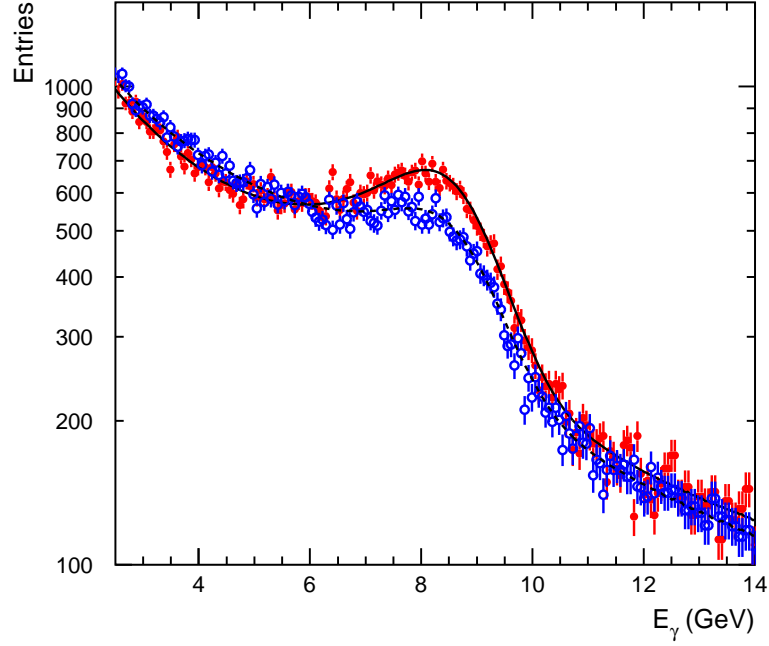


**Figure 8.** Experimental energy spectra of a given bunch corresponding to  $S_3 = 1$  (full dots) and  $S_3 = -1$  (open dots). Each spectrum was accumulated during about 10s of acquisition time. The fit results are also shown (the full and dashed curves).

## 5. HERA Running and Cavity Data Taking

The total LPOL cavity data taking amounts to about 500 hours (from 6 October 2006 to the end of the HERA running in June 2007).

It is important to consider the operating conditions because they happen to differ vastly from the foreseen ones. As a consequence the real analysis method had to be modified or improved in various situations.

*HERA beam orbit instabilities:* Usually the electron beam was very stable, but occasionally it suffered from rapid changes as can be seen in Fig. 9 where the beam conditions changed between the  $S_3 = -1$  and  $S_3 = +1$  spectra measurements. Two more parameters were then added to the likelihood estimate to account for a different BCP and BGP fluxes in the  $S_3 = -1$  and  $S_3 = +1$  energy spectra. In this particular example, the BGP flux has varied by 40% while the BCP flux remains unchanged. For the polarisation measurement, the variation of both fluxes is required to be less than 20% which rejects only a small fraction of spectra (less than 0.4%).

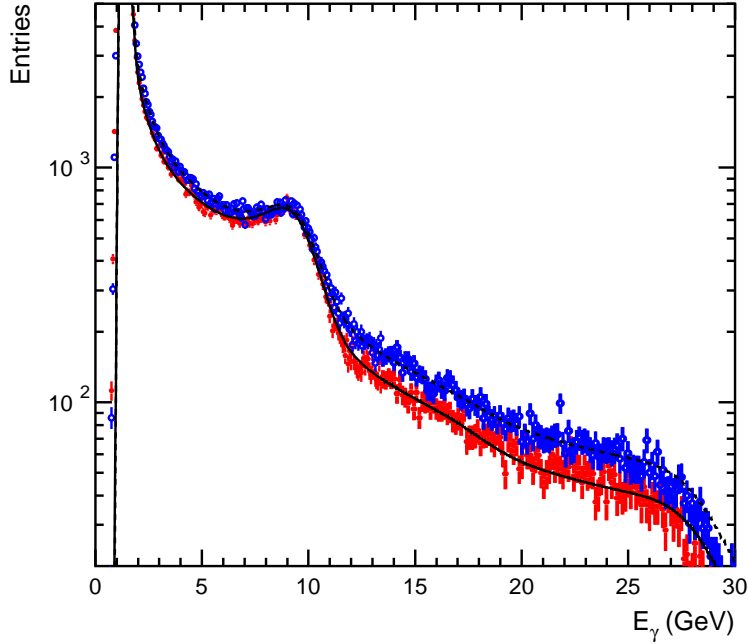


**Figure 9.** Energy spectra showing the beam instability between the  $S_3 = -1$  (open dots) and  $S_3 = +1$  (full dots) spectra measurements. Each spectrum was accumulated during about 10s of acquisition time. The curves represent the corresponding fit results.

*HERA beam orbit slow variations - calorimeter exposure:* From fill to fill and even during a fill, the orbit may change and hence so does the impact on the calorimeter of the BCPs (and BGPs). As the calorimeter is very narrow and leakage may happen, this may induce changes in the detector parameters governing energy scale and resolution. This is why detector parameters are reestimated on the histograms themselves by a MINUIT optimisation procedure every 3 minutes (20 data acquisition samples).

*Radiative peak position:* The synchrotron radiation flux, being generated by the magnetic fields on the electron trajectory, is sensitive to orbit changes. Therefore, one more parameter is needed to describe its average energy  $E_{\text{SRP}}$ . This parameter defines the histogram position on the energy scale and is determined by a parabolic fit to the maximum of every energy histogram. One expects a correlation between the electron beam current and  $E_{\text{SRP}}$ . The larger  $E_{\text{SRP}}$  the higher the level of synchrotron radiation. This is indeed what we have observed (Fig. 10). It should be pointed out that during the commissioning phase the synchrotron radiation level was found to be much higher than was foreseen; this was finally traced back to the transverse magnetic field applied to the gaseous fixed target in the HERMES experiment from 2001 till the end of 2005.

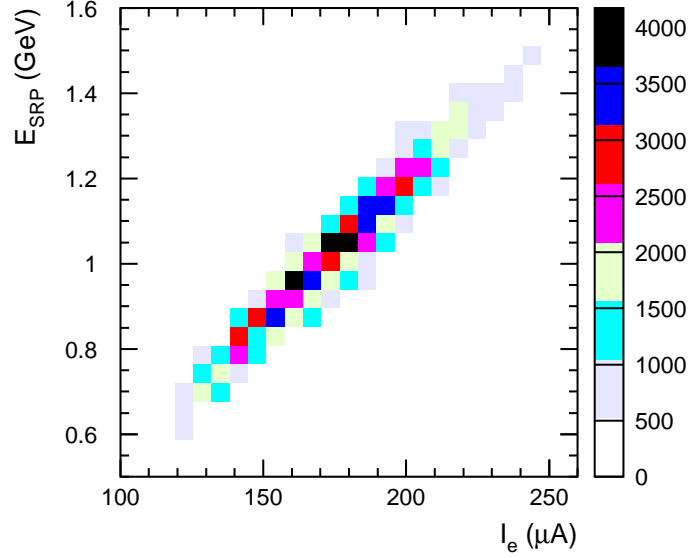


**Figure 10.** Observed correlation between the bunch-dependent electron beam current and the synchrotron radiation level ( $E_{\text{SRP}}$ ).

*Electronic sampling subtraction:* Figure 11 shows histograms of bunches 1 and 2 of the HERA beam: Bunch 2 shows a structure below the radiation peak. This happens for full data acquisition runs representing about 40% of the whole sample. It is due to a timing uncertainty at the start of data acquisition system: the signal is extracted from the maximum ADC sample of one bunch and the minimum ADC sample (baseline) from the previous bunch (see Sect. 3.3.2) instead of the subtraction of two ADC samples within one bunch. This results in a measured energy which is spoiled by the still active decay of the preceding bunch signal after half an HERA clock (48 ns). The measured energy is thus in this case

$$E = E_{\text{bunch}} - a_{\text{pileup}} E_{\text{bunch}-1}, \quad (5.1)$$

where  $a_{\text{pileup}}$  is an attenuation parameter. For the analysis, the bunches are treated chronologically and the likelihood procedure always starts after empty bunches. The energy spectrum of the first non-empty bunch (bunch 1) can thus be determined precisely without any correction. The energy spectrum of the next bunch (bunch 2) is corrected by a convolution with

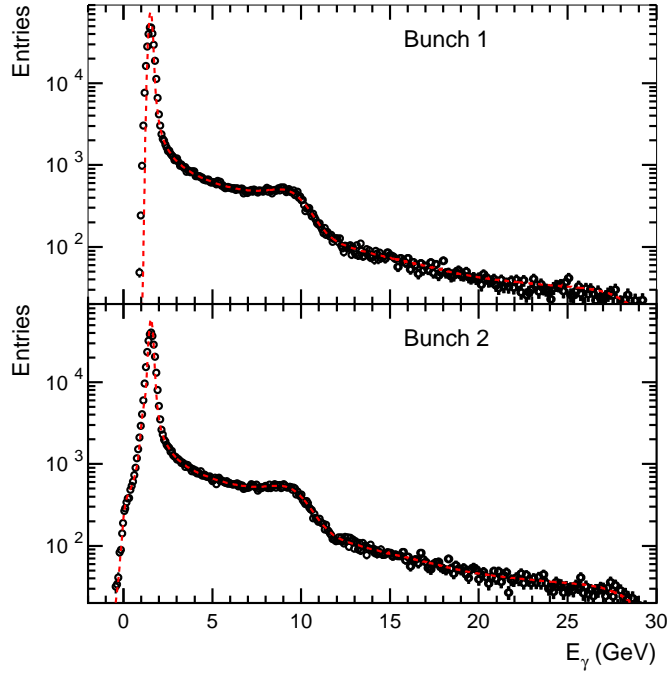


**Figure 11.** Difference in energy spectra between bunches 1 and 2 showing the pileup effect in bunch 2. The open dots show the data and the curves the fit results.

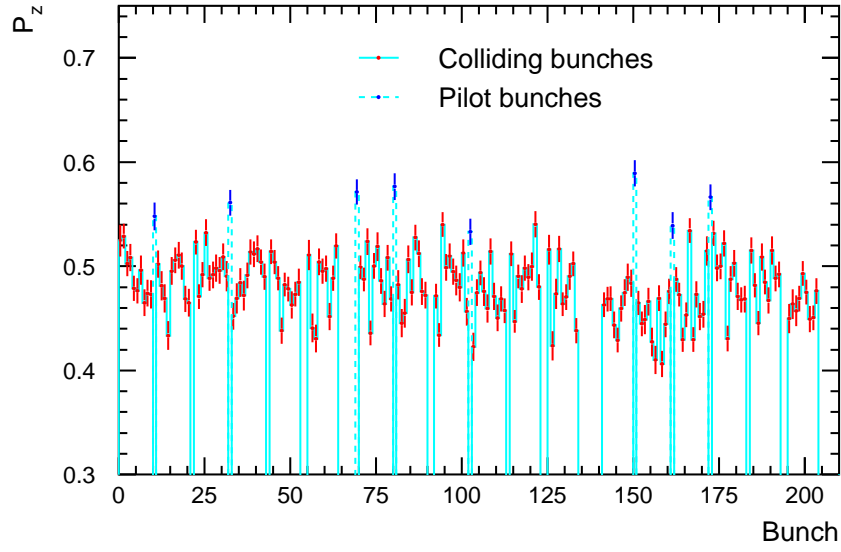
the previous energy spectrum, according to Eq.(5.1), and so on for the following bunches. After optimisation on a selected sample from the affected data we get a precise estimate of the attenuation parameter  $a_{\text{pileup}} = 0.057 \pm 0.002$ . This parameter remained constant within  $\sim 10\%$  for all data taking.

## 6. Results of Polarisation Measurement

All LPOL cavity data have been analysed with the polarisation results available to be compared with the corresponding measurements from the TPOL. Here a few selected results are shown.

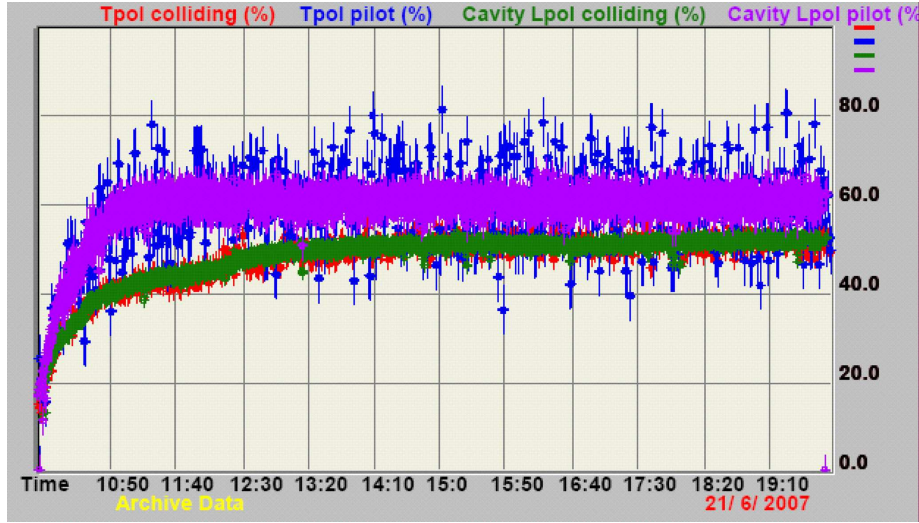
The LPOL cavity provides a bunch dependent polarisation measurement every 20s. The relative statistical precision is about 2% per bunch per minute as shown in Fig. 12 for a typical example. In addition to the bunch structure, one also observes a significant bunch-to-bunch polarisation variation, not only between the colliding and non-colliding (pilot) bunches but also among the colliding bunches.

Figure 13 shows an example of online polarisation measurements of one HERA luminosity fill provided by the LPOL cavity and TPOL polarimeters for both the colliding and pilot electron bunches. The online measurements of the LPOL cavity were based on the same method as for offline measurements described in previous sections. The better statistical precision from the LPOL cavity polarimeter can be clearly appreciated. Figure 13 also shows that the polarisation values differ significantly between the colliding bunches and pilot bunches. Within the colliding bunches, the beam-beam effect is expected to vary depending on the proton bunch current, whereas such effect



**Figure 12.** Bunch dependent polarisation measurement from the LPOL cavity averaged over 3 independent measurements corresponding to about one minute duration. The error bars represent the statistical precision of the measurement with the solid (dashed) histograms showing the colliding (pilot) bunch structure.

is absent for the pilot bunches. These differences are indeed observed from the bunch dependent polarisation measurement.



**Figure 13.** Online polarisation measurements from the LPOL cavity (green and purple for the colliding and non-colliding (pilot) electron bunches, respectively) and the TPOL (red and blue).

Figure 14 shows the dependence of the polarisation as a function of the proton beam current  $I_p$  for a long HERA fill. The data are split into three bins of the time since the start of the fill. Here the colliding bunches have non-zero proton beam current  $I_p \neq 0$  and the pilot bunches are located at  $I_p=0$ . Within the colliding bunches, one sees a dependence on  $I_p$  which is strong in



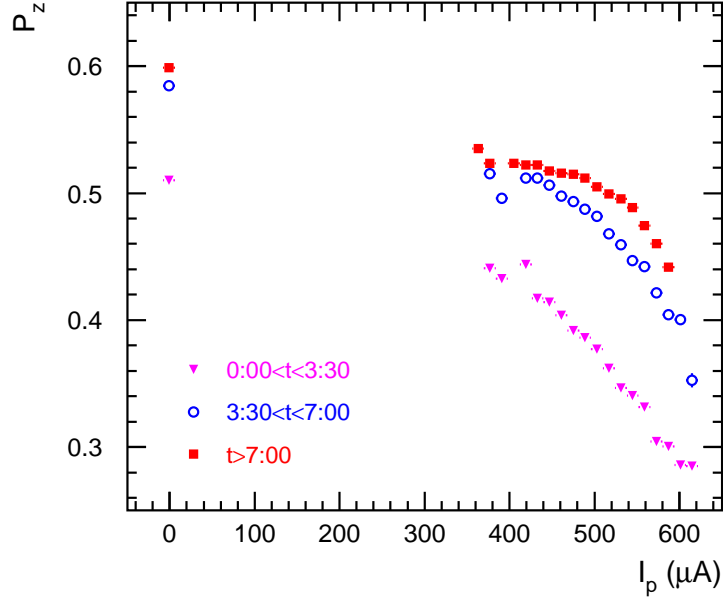


**Figure 14.** Measured polarisation dependence on the bunch-dependent proton beam current and the time evolution.

the first half of the fill but becomes weaker in the second half. The bunch dependent polarisation measurements provided by the LPOL cavity allow the incorporation of all these effects into the relevant measurements at HERA.

At the end of the HERA operation, some dedicated runs were taken with the proton beam unfilled and the electron beam undergoing a total of 13 rise-time periods. For each period,  $P_z^\infty$ ,  $\tau$  and  $P_z^0$  (the polarisation at the beginning of the period) were extracted using the averaged polarisation of all filled electron bunches with an estimated polarisation uncertainty  $< 0.2\%$ . The averaged polarisation  $P_z(t)$  of each period was fitted using the formula

$$P_z(t) = P_z^\infty + (P_z^0 - P_z^\infty) e^{-\frac{t}{\tau}}. \quad (6.1)$$

One period is shown in Fig. 15 where the data points correspond to the LPOL cavity measurements and the dashed curve the fit. Towards the end, the beam was depolarised for starting a new rise-time period. Both the rise and rapid falling of polarisation were precisely measured. Figure 16 shows the plot of  $P_z^\infty$  versus  $\tau$  for the 11 long rise-time periods. The straight line shows the ST prediction (Eq.(2.4)), the result,  $P_z^\infty/\tau = 0.02537 \pm 0.00004 \text{ (min}^{-1}\text{)}$ , is about one standard deviation away from the expectation.

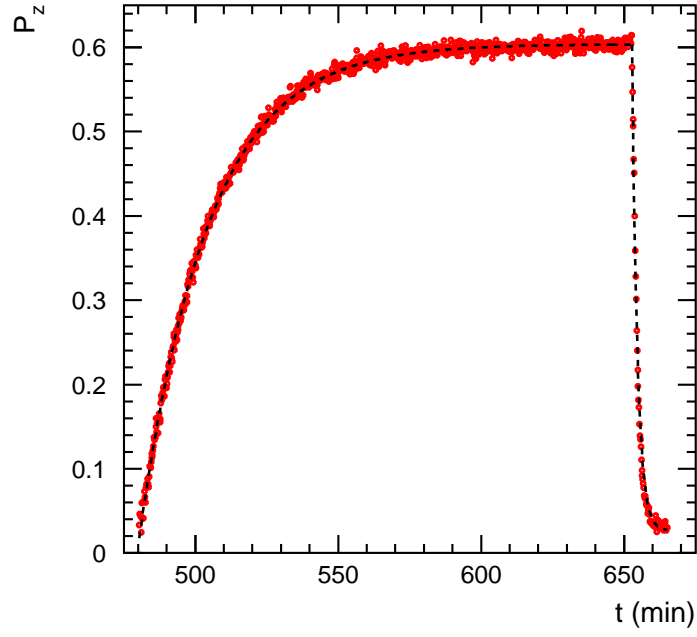


**Figure 15.** One example of the rise-time periods with the data points showing the LPOL cavity measurements and the dashed curve the corresponding fit.

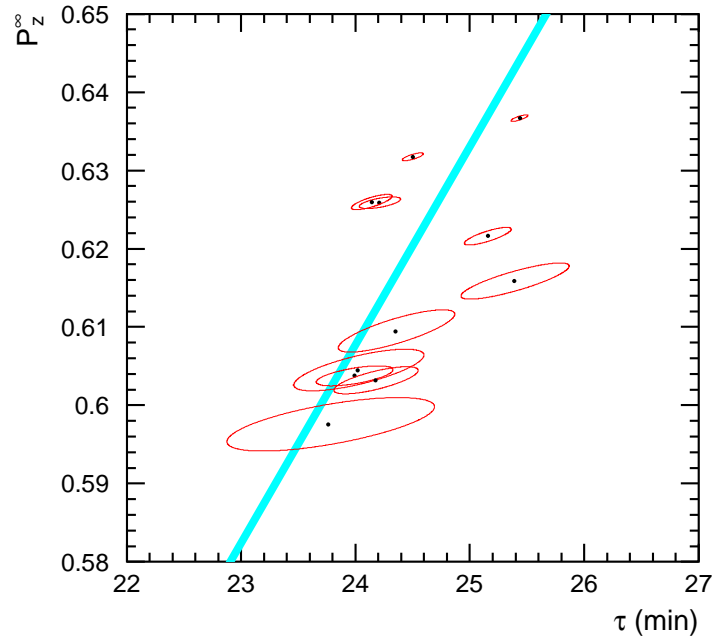


**Figure 16.** The fitted correlation between the maximum polarisation value  $P_z^\infty$  and the intrinsic rise-time  $\tau$  for the 11 long periods (ellipses) out of 13 in total, in comparison with the expectation (straight line).

## 7. Systematic Studies

Detailed systematic studies have been performed using the full LPOL cavity data set, including

dedicated data taking periods with non-standard setups. Among different systematic sources, we distinguish two types of uncertainties: one type (uncorrelated systematic error) which is present for every single measurement but becomes negligible for a large integrated data sample since it behaves as a statistical uncertainty; the other type (correlated systematic error) which is common for all the measurements.

## 7.1 Uncorrelated Systematic Errors

**Systematics affecting independently each HERA fill (HERA beam variations):** The direction of the electron beam and the impact of the BCPs on the calorimeter affect the calorimeter response leading to systematics. A devoted scan changing the beam position and angle in the horizontal plane gives an error limit of 0.4%. However, to a first approximation this has to be divided by the square root of the number of fills (which represents about 100 fills for the LPOL cavity data taking), thus becoming negligible.

**Systematics related to detector parameters:** Each data acquisition lasts for about 10 seconds recording 220 energy spectra for each bunch for a given laser polarisation, which is either left-handed or right-handed. The laser swapping frequency is matched with that of the data acquisition system. Every 20 data acquisition samples defines a microperiod. For each microperiod, a MINUIT fit is performed to define detector parameters using the measured spectra from those bunches which have at least three empty preceding bunches (thus the spectra are unaffected by the observed pileup feature mentioned in Sect. 5).

To check the effect of the uncertainty of the fitted detector parameters, two independent methods are used:

- The parameters are varied according to the eigenvectors of the MINUIT Hessian matrix. The polarisations are refitted with the new sets of parameters.
- The polarisations are simply refitted with the set of parameters determined from the next microperiod.

Both methods agree and give a relative uncertainty on the polarisation measurement of about 0.5%. The corresponding systematic error is thus negligible due to more than 9000 microperiods of the LPOL cavity data taking.

## 7.2 Correlated Systematic Errors

**The BGP and BBP cross-sections:** They depend on the residual gas composition for BGP and on the beam pipe temperature for BBP. Simulating a variation of these data has shown that the induced systematics is negligible.

**Calorimeter resolution and ADC to energy conversion parameterisations:** The parameterisation used for describing calorimeter resolution and ADC to energy conversion were partially inspired from the (GEANT3) simulation. For the energy conversion, the possibility of leakage was taken into account. In fact, four other forms of parameterisation for the energy conversion were used and another Gaussian-like one was also tried for energy resolution. The 10 possibilities have

been tested on a 1.5% data subsample equally distributed over the full sample and representing different situations such as high and low BCP, BGP and SRP rates. The solution retained was the one giving the best overall likelihood estimator, i.e. the expression of Eqs.(4.5) and (4.6). The polarisation differences between the best solution and three other good possibilities lead to a systematic error estimate of 0.4%.

**Merging of the SRP peak:** The likelihood estimator is very sensitive to the synchrotron radiation peak region (accounting for  $\approx 80\%$  of the recorded entries per histogram) which means that it is more affected by its fluctuations than by the other interesting photons. Hence a merging of the energy histogram bins in this region was made in order to reduce the effect while keeping the histogram number of entries constant. By changing the way the bin merging is made a systematic error of 0.4% has been found on the used data subsample.

**Left and right laser beam polarisations:** The circular laser beam polarisation  $S_3$  has been measured using the optical ellipsometer with an uncertainty of 0.3% [26]. This has been however checked by a devoted scan measurement: in a period of time short enough to expect that the electron polarisation will only change slowly, five different MOCO position combinations have been used to measure the polarisations. Each combination corresponds to a different degree of circular laser polarisation. The analysis of the scan data leads to a systematics error consistent with the above value.

**Electronic sampling subtraction:** The same attenuation factor  $a_{\text{pileup}}$  has been used for all the data samples. In fact it has been measured only on a dedicated subsample. Its size and stability showed no necessity to have another strategy. For the whole sample the policy was to measure the polarisation imposing  $a_{\text{pileup}} = 0$  and calculate the correction by use of the dedicated subsample. In fact some dependence of the correction with respect to the BGP and BCP yields was found and used. Taking into account the width of  $a_{\text{pileup}}$ , the estimated error on the correction and the relative number of affected measurements, the corresponding systematic error has been estimated to be 0.4%.

**Calorimeter position scan:** In the nominal data taking, the calorimeter is centered around the scattered photon beam line. During a dedicated run, the calorimeter has been moved both vertically and horizontally. The polarisation measurement is found to be stable within 0.4% for both directions.

### 7.3 Overall Systematic Uncertainty

The systematic uncertainties of all considered error sources are summarised in (Table 1). It should be pointed out however that

- The scan analysis method assumes the polarisation to vary linearly with time during the scan and the scan is performed in a relatively short period of time. This induces an intrinsic investigation limit of  $\sim 0.5\%$  so the real value of the error could (and sometime is expected to) be much smaller.
- The uncorrelated errors should be added in quadrature but here some are correlated in a somewhat uncertain way. This renders the summing process also rather uncertain.

**Table 1.** Estimation of the relative systematic errors of the LPOL cavity polarimeter for an individual polarisation measurement.

Source	$\Delta P/P(\%)$
Uncorrelated errors	
HERA beam variations	0.4
Detector parameters	0.5
Correlated errors	
BGP and BBP cross-sections	negligible
Calorimeter resolution and ADC to energy conversion	0.4
Merging of the SRP peak	0.4
Laser polarisation circularity	0.3
Electronic sampling subtraction	0.4
Calorimeter position scan (horizontal)	0.4
Calorimeter position scan (vertical)	0.4

Bearing all that in mind an overall relative systematic error of 0.9% is quoted on the LPOL cavity polarisation measurement for a large integrated period. For an individual measurement in a short time period, the corresponding uncertainty is 1.1%.

## 8. Summary

A new polarimeter for precisely measuring the longitudinal polarisation of the electron beam at HERA has been constructed and successfully operated. The polarimeter employs a Fabry-Perot cavity for enhancing the laser intensity by more than three orders of magnitude so that the electron-photon interaction rate is sufficiently large to reach the few photon mode. A fast data acquisition system has also been developed to record all back-scattered photons produced every 96 ns for every electron bunch.

The measurement of the electron beam polarisation is reported for the first time in the few photon mode leading to a statistical precision of 2% per bunch per minute. This offers an improvement over the other two HERA polarimeters which are limited by either lower laser intensity or smaller electron-photon interaction rate.

Detailed systematic studies have been performed resulting in a total relative systematic uncertainty of about 1%, which is a factor of 2 – 3 smaller than the precision quoted currently by the other polarimeters at HERA. To reach such a small systematic uncertainty, we have used the possibility to describe the few photon energy spectra from first principles by convoluting the signal and background QED processes with the detector effects. Our major observation is that the detector parameters, used to relate the theoretical energy spectra to the measured ones, could be determined once every 3 minutes of data taking independently of the electron beam polarisation measurement. This allowed us to account for detector response variations as functions of the photon entrance position in the calorimeter and aging effects.

These precise polarisation measurements can be used as a reference to cross-calibrate the other polarimeters and to help resolve some of the remaining discrepancies observed between the two other HERA polarimeters.

## Acknowledgment

We are grateful to all members of the POL2000 group for their support and discussions. The support from the HERA machine group, and the H1, HERMES and ZEUS experiments is also warmly acknowledged. We thank A. Airapetian, M. Ait-Mohand, C. Cavata, I. Cheviakov, R. Fabbrì, M. Hensel, Y. Holler, M. Klein, J. Ludwig and C. Vallée for their help at different stage of the project.

## References

- [1] The H1 experiment, see <http://www-h1.desy.de/>.
- [2] The ZEUS experiment, see <http://www-zeus.desy.de/>.
- [3] The HERMES experiment, see <http://www-hermes.desy.de/>.
- [4] H. Kogelnik and T. Li, *Laser beams and resonators*, *Proc. of the IEEE* **54** (1966) 1312.
- [5] M. Beckmann *et al.*, *The longitudinal polarimeter at HERA*, *Nucl. Instrum. Meth.* **A479** (2002) 334.
- [6] D.P. Barber *et al.*, *The HERA polarimeter and the first observation of electron spin polarization at HERA*, *Nucl. Instrum. and Meth.* **A329** (1993) 79.
- [7] HAPPEX collaboration, N. Falletto *et al.*, *Compton scattering off polarized electrons with a high finesse Fabry-Perot cavity at JLab*, *Nucl. Instrum. Meth.* **A459** (2001) 412.
- [8] M. Baylac *et al.*, *First electron beam polarization measurements with a Compton polarimeter at Jefferson Laboratory*, *Phys. Lett.* **B539** (2002) 8.
- [9] S. Escoffier *et al.*, *Accurate measurement of the electron beam polarization in JLab Hall A using Compton polarimetry*, *Nucl. Instrum. Meth.* **A551** (2001) 563.
- [10] S. Baudrand-Ouadi, *Mesure de la polarisation longitudinale de faisceaux de positons et d'électrons à HERA par effet Compton à l'aide d'une cavité Fabry-Perot de haute finesse*, PhD thesis, LAL 07-14, Univ. Paris-Sud (2007).
- [11] A.A. Sokolov and I.M. Ternov, *On polarization and spin effects in the theory of synchrotron radiation*, *Sov. Phys. Doklady* **8** (1964) 1203; I.M. Ternov, Yu.M. Loskutov and L.I. Korovina, *Possibility of polarizing an electron beam by relativistic radiation in a magnetic field*, *Sov. Phys. JETP* **14** (1962) 921.
- [12] D.P. Barber, *Electron and proton spin polarization in storage rings: an introduction*, [Physics/9901038].
- [13] D.P. Barber, *Polarized Electron Beams in Storage Rings*, DESY Internal Report, DESY M 96-17 (1996).
- [14] J. Buon and K. Steffen, *HERA variable energy 'mini' spin rotator and head-on ep collision scheme with choice of electron helicity*, *Nucl. Instrum. and Meth.* **A245** (1986) 248.
- [15] M. Placidi and R. Rossmanith,  *$e^+e^-$  polarimetry at LEP*, *Nucl. Instr. and Meth.* **A274** (1989) 79.

- [16] Y. Mizumachi *et al.*, *Transverse electron beam polarimetry in TRISTAN main ring*, KEK-89-141 (1989).
- [17] R. King, *A precise measurement of the left right asymmetry of Z boson production at the SLAC linear collider*, PhD Thesis SLAC 1994, SLAC-Report-452; A. Lath, *A precise measurement of the left-right cross section asymmetry in Z boson production*, PhD Thesis SLAC 1994, SLAC-Report-454;
- [18] D. Blockus *et al.*, *Proposal for polarization at the SLC*, SLAC-Proposal-SLC-Upgrade-01(1986).
- [19] U. Fano, *Remarks on the classical and quantum-mechanical treatment of partial polarization*, *J. Opt. Soc. Am.* **39** (1949) 859.
- [20] T. Suzuki, *General formulae of luminosity for various types of colliding beam machines*, KEP-76-3 (1976).
- [21] J. Limpert *et al.*, *High repetition rate gigawatt peak power fiber laser systems: challenges, design, and experiment*, *IEEE J. Sel. Quant. Elec.* **15** (2009) 159.
- [22] R.J. Jones and J.C. Diels, *Stabilization of femtosecond lasers for optical frequency metrology and direct optical to radio frequency synthesis*, *Phys. Rev. Lett.* **86** (2001) 3288.
- [23] A.E. Siegman, *Lasers*, University Science books (1986).
- [24] D.Z. Anderson, *Alignment of resonant cavities*, *Appl. Opt.* **23** (1984) 2944.
- [25] T.J. Kane and R.L. Bayer, *Monolithic, unidirectional single-mode Nd:YAG ring laser*, *Opt. Lett.* **10** (1985) 65.
- [26] V. Brisson *et al.*, *Per mill level control of the circular polarisation of the laser beam for a Fabry-Perot cavity polarimeter at HERA*, *JINST* **5** P06006 [arXiv:1005.2742 [physics.ins-det]].
- [27] C. Scarlett and W. Lorenzon, *A new sampling calorimeter for the longitudinal polarimeter at HERMES*, Oct. 2000.
- [28] R. Brun *et al.*, *GEANT: Simulation program for particle physics experiments, user guide and reference manual*, <http://cdsweb.cern.ch/record/1119728>.
- [29] V. Boudry *et al.*, *The electronics of the new H1 luminosity system* in proceedings of *International Conference on Calorimetry in HEP*, 25-29 March 2002, Pasadena.
- [30] Creative Electronic System: <http://www.ces.ch>.
- [31] F. Zomer, *Habilitation thesis, A high power Fabry-Perot resonator for precision Compton polarimetry with the longitudinal polarised lepton beams at HERA*, LAL 03-12 (2003) [<http://publication.lal.in2p3.fr/2003/LAL03.12.pdf>].